Potential response of single successive constant-current-driven electrolytic hydrogen bubbles spatially separated from the electrode

Akash Raman [*],[1],[a], Pablo Peñas [1],[b], Devaraj van der Meer [b], Detlef Lohse [b], Han Gardeniers [a], David Fernández Rivas [a]

[a] *Mesoscale Chemical Systems Group, MESA+ Institute for Nanotechnology, Faculty of Science and Technology, University of Twente, P.O. Box 217, Enschede 7500 AE, the Netherlands*
[b] *Physics of Fluids Group and Max Planck Center Twente, MESA+ Institute and J. M. Burgers Centre for Fluid Dynamics, Faculty of Science and Technology, University of Twente, P.O. Box 217, Enschede 7500 AE, the Netherlands*

ARTICLE INFO

ABSTRACT

The presence of bubbles in gas-evolving electrolytic processes can heavily alter the mass transport of gaseous products and can induce severe overpotential penalties at the electrode through the action of bubble coverage (hyperpolarization) and electrolyte constriction (Ohmic shielding). However, bubble formation can also alleviate the overpotential by lowering the concentration of dissolved gas in the vicinity of the electrode. In this study, we investigate the latter by considering the growth of successive hydrogen bubbles driven by a constant current in alkaline-water electrolysis and their impact on the half-cell potential in the absence of hyperpolarization. The bubbles nucleate on a hydrophobic cavity surrounded by a ring microelectrode which remains free of bubble coverage. The dynamics of bubble growth does not adhere to one particular scaling law in time, but undergoes a smooth transition from pressure-driven towards supply-limited growth. The contributions of the different bubble-induced phenomena leading to the rich behaviour of the periodic fluctuations of the overpotential are identified throughout the different stages of the bubble lifetime, and the influence of bubble size and applied current on the concentration and Ohmic overpotential components is quantified. We find that the efficiency of gas absorption, and hence the concentration-lowering effect, increases with increasing bubble size and also with increasing current. However, the concentration-lowering effect is always eventually countered and overcome by the effect of Ohmic shielding as the bubble size outgrows and eclipses the electrode ring beneath.

1. Introduction

The global effort to achieve carbon neutrality and the falling cost and increasing reliability of renewable energy has opened new possibilities for chemical industries [1,2]. There has been increased attention on process electrification and the opportunity to replace or augment existing chemical processes with electrochemical synthesis alternatives [2–8]. In particular, hydrogen generation from electrochemical water-splitting is a promising source of future renewable energy [9–11]. Bubbles unavoidably form on the electrodes of many important gas-evolving electrochemical processes, such as water electrolysis, the chlor-alkali process and the Hall-Heroult process [12–19]. The importance of understanding how electrolytic bubbles impact the mass transfer and energy efficiencies of electrochemical cells is reflected in

the growing number of publications on the topic [20,21]. The lifetime of a surface-bound bubble can be understood as a sequence of three events: bubble nucleation, bubble growth, and bubble detachment. Upon the start of electrolysis, the gas molecules generated at the electrodes dissolve into the electrolyte. The local gas-supersaturation of the surrounding electrolyte eventually becomes sufficiently large for bubble nucleation on the electrode surface and subsequent bubble growth [22–25]. Naturally, the bubble growth rate increases with the current density applied [26,27]. The growth kinetics of electrolytic bubbles is well documented and it is commonly expressed in the form of the general equation.

$$R_b = \beta t_b^{\alpha}, \tag{1}$$

where R_b is the bubble radius, t_b the time since nucleation; α is referred

---

to as the time exponent and β as the growth coefficient. Three distinct growth regimes have been reported based on the value of α. First, there is a pressure-driven regime during which the bubble radius increases linearly in time ($\alpha = 1$) [28,29]. In the case of bubbles growing on electrodes much larger than the bubble radius at detachment, a diffusion-limited regime ($\alpha = 1/2$) follows, where growth is controlled by diffusion from the gas-oversaturated bulk electrolyte to the bubble [26,27,30]. In contrast, a reaction-limited growth regime is observed throughout the entire lifetime of the bubble when gas production is localised at the foot of the bubble—as is the case for micro- and nano-electrodes [31–35]. Virtually all gas evolved at the electrode ends up in the bubble, mostly by coalescence with smaller microbubbles. Therefore, the bubble grows at a constant volumetric growth rate ($\alpha = 1/3$) when generated under constant-current conditions. The production-limited regime also applies to the growth of plasmonic bubbles in gas-equilibrated water [36], albeit under a thermal gas-generation mechanism. For the electrolytic case, recent evidence suggests that the emerging bubbles rest atop a permanent carpet of microbubbles [37]. For high enough electric potentials, the competition between buoyancy and the (carpet-dependent) electric force results in oscillatory growth. Bubbles can affect the total electric potential drop across the electrolytic cell in both desirable and detrimental ways. For example, microconvective flows generated during bubble growth, coalescence and departure alleviate the gas-concentration overpotential by enhancing the mass transfer of dissolved gas away from the electrode surface [38–40]. On the other hand, electrolytic bubbles increase the Ohmic penalty in two important ways. Firstly, bubbles adhering to the electrode surface block an area of the electrode, rendering it electrochemically inactive. During chronopotentiometry, the reduced electrode surface must admit larger current densities from which a larger activation overpotential (associated with the electrode kinetics) arises. This effect is often referred to as hyperpolarization [40,41]. The extent of bubble surface coverage—hence hyperpolarization—is greatly influenced by the aerophobicity and porosity of the electrode surface [42–44], and increases with current density [45]. Secondly, bubbles cause further Ohmic losses in the electrolyte by blocking ion conduction pathways (in the electrolyte) and constricting the passage of current [45–47]. On the contrary, it has been recently shown that bubbles growing directly on electrode surfaces (note that this is not the case in the system used in this study) can act as ion conduction pathways themselves [48–50]. Although the separation of the concentration and hyperpolarization overpotentials has been quantified for other electrochemical systems with larger electrodes and stochastic bubble generation [51,52], the effect of single bubbles on the individual overpotential components still remains elusive. In this study, we aim to bridge this gap by observing successive electrolytic bubbles in a recent cell design where the site of bubble nucleation is separated from the site of gas generation. We restrict the study to currents below 50 µA to ensure that bubbles do not nucleate on the electrode. Therefore, hyperpolarization

losses—which could otherwise be predominant—are avoided. The half-cell overpotential then strictly suffers from the more subtle Ohmic and concentration overpotential losses induced by the action of a single bubble; their quantification and understanding is the main objective of this work. The paper is organised as follows. Section 2 describes the electrolysis cell and the experimental method. In Section 3 we first present the growth of the single-bubble successions and the synchronous fluctuations in the half-cell overpotential. The bubble growth dynamics are subsequently explored in Section 3.1, followed by the efficiency of gas evolution in Section 3.2. Section 3.3 discusses the different stages in the overpotential fluctuations in relation to the different bubble-induced phenomena. The discussion is further developed in Section 3.4, where the effect of the bubble size and the current density on the Ohmic, and the concentration overpotential components are quantitatively estimated by means of a steady-state numerical model. Finally, the paper concludes with a summary of the main findings and an outlook in Section 4.

2. Materials and methods

2.1. Experimental setup

The cathode-containing samples were fabricated using 525 µm thick, boron-doped silicon substrates 10×10 mm^2 on which a platinum ring (ring inner radius $r_i = 230$ µm, outer radius $r_o = 255$ µm, 90 nm deep with a 10 nm adhesion layer) encircles a 25 µm deep, pit (radius $r_p = 10$ µm). The pit is made hydrophobic by the conformal deposition of fluorocarbons. This process has been previously shown to result in a fluorocarbon layer with surface properties similar to polytetrafluoroethylene (PTFE) [53]. The hydrophobicity of the cavity is further enhanced by the creation of black silicon structures at the bottom [54]. Sputter deposited platinum has previously been shown to be hydrophilic [55,56]. The back side of the substrate is coated with platinum and this provides an electrical contact to the Pt ring via the highly-doped silicon. A 100 nm silicon dioxide layer at the top ensures that only the ring electrode conducts current to the electrolyte. A schematic of the substrate and set-up is shown in Fig. 1. The fabrication steps are specified in greater detail in Supplementary Information SI1, Section S6. The substrates were placed in a custom 3D-printed holder and sealed using an O-ring. A spring plunger screw in the holder was used to provide external circuit connections. The holder has an angled port where a reference electrode can be placed ≈ 3 mm away from the pit and sealed with an O-ring. An Ag/AgCl electrode in saturated KCl (Pine Research) is used as reference electrode in all experiments. This was absent in the setup used in the previous work by Peñas et al. [57]. A platinum wire electrode (BASi Inc. MW-1032) acts as the counter electrode. The immersed area of the counter electrode is ≈ 500 times larger than the ring electrode area. This ensures that the current density at the counter electrode is small compared to that at the cathode. The electrodes are
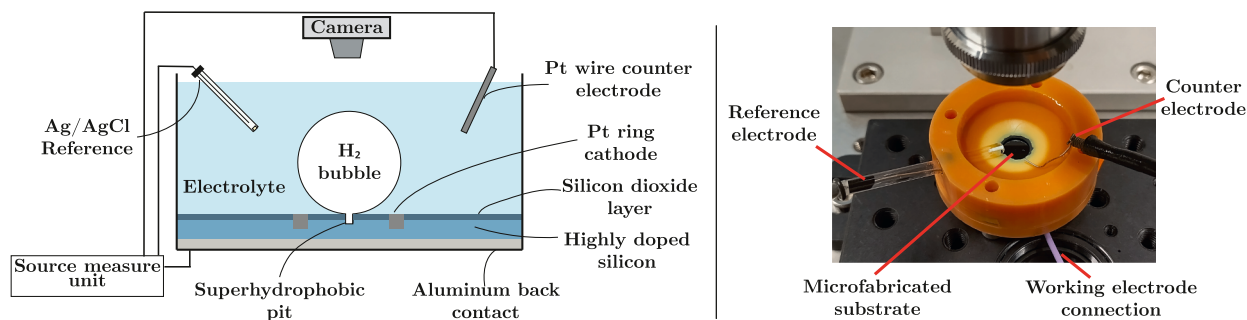

Fig. 1. Left panel: Sketch of the three-electrode electrolysis cell. A constant current is applied between the platinum ring (working electrode) and a platinum wire (counter-electrode). Bubbles are generated selectively at a hydrophobic pit etched at the Si substrate at the centre of the platinum ring. Right panel: Annotated image of experimental electrolysis cell. A circular area of the microfabricated substrate is exposed to the electrolyte and is visible as a dark circle in the illuminated area. The platinum ring electrode (not visible at this scale) is at the center of the substrate and is connected to the source measure unit (SMU) via back contact.

connected to a Keithley 2410 Source Measure Unit (SMU). The holder is filled with 4 mL of 0.1 M NaHCO$_3$ electrolyte which is not degassed and remains open to and in equilibrium with the gases constituting the atmosphere throughout the experiments.

2.2. Chronopotentiometry experiment

Chronoamperometric experiments were conducted at currents i = 10, 20, 30, 40 and 50 µA applied between the Pt-ring cathode and the Pt-wire anode. The half-cell voltage E is measured between the Pt-ring cathode and the reference electrode. Our quantity of interest is the total overpotential E_t for the hydrogen evolution reaction, which corresponds to the half-cell potential referenced to a reversible hydrogen electrode (RHE). It can be computed from the measured voltage by means of the Nernst equation [58,59],

$$E_t = E + 2.3 \frac{\mathscr{R}T}{F} \text{pH} + E_{RE}. \tag{2}$$

Here, $E_{RE} = +0.199$ V is the potential of the reference electrode (vs. the standard hydrogen electrode), $\mathscr{R}$ the universal gas constant, T the absolute temperature, F the Faraday constant and the electrolyte has pH = 8.5. The half-cell overpotential amounts to $E_t = E + 0.70$ V in our case; note that E_t is a negative quantity. A custom LabVIEW Virtual Instrument (VI) was made to acquire and display data from both the SMU and the camera simultaneously. Images were recorded at 5 fps at a resolution of $\approx$ 1.7 µm/pixel. Fig. 2 shows raw and processed experimental frames at different stages of bubble nucleation and growth. It should be pointed out that the bubble radius R_b corresponding to frame C (red marker) falls just outside the (corrected) growth curve of the bubble. This offset is caused by the optical interference of the bright ring with the darker bubble contour. It is corrected through gradient interpolation (see Supplementary Information, SI1 Section S1) in the interval $r_i \leq R_b \leq r_o$ during which the bubble is outgrowing the ring electrode below.

3. Results and discussion

The time evolution of the half-cell overpotential E_t and the corresponding bubble growth dynamics are shown in Fig. 3 for a set of typical experiments comprising five different currents. Bubble growth from the hydrophobic pit is successive—a new bubble nucleates immediately after the detachment of the previous one. As expected, increasing the current density results in faster bubble growth and in a higher frequency of bubble departure. It is worth pointing out that the long initial gap absent of bubbles in the plot for $i = 20$ µA arises because a few spurious bubbles nucleating at the ring (not shown) delayed successive bubble growth at the pit in that particular experiment. In addition, in the plots for 30 and 40 µA, small bubbles are seen at the pit during the first 50 s. These bubbles detach early because they coalesce with spurious bubbles that form on the ring at higher currents at the start of electrolysis. It is worth pointing out that only bubbles growing at the pit and in the absence of other spurious bubbles are considered for further analysis. Firstly, bubbles that coalesce with spurious bubbles are filtered by excluding bubbles departing at radii <400 µm. Secondly, only bubbles with geometric centres within 15 pixels of the center of the pit are considered for analysis. Aside from these anomalies, the growth frequency and detachment sizes remains reasonably homogeneous throughout the vast majority of bubbles in the succession. The variations in the bubble departure radius are discussed in the electronic supplementary information (SI1 Section S3), whereas the growth dynamics shall be addressed further in the next section, Section 3.1.

On another note, the periodic fluctuations of $E_t(t)$ are synchronous with the growth and detachment of the bubble, yet their nature depends strongly on the applied current (see Fig. 3, right panels). Nonetheless, we distinguish two broad features that correspond well with previous reports [41,52,57,60,61]. First, the overpotential increases (i.e., becomes more negative) as the bubble grows larger. Second, bubble departure is always accompanied by a sharp drop in E_t. The underlying phenomena giving rise to these and other intricate features of $E_t(t)$ will
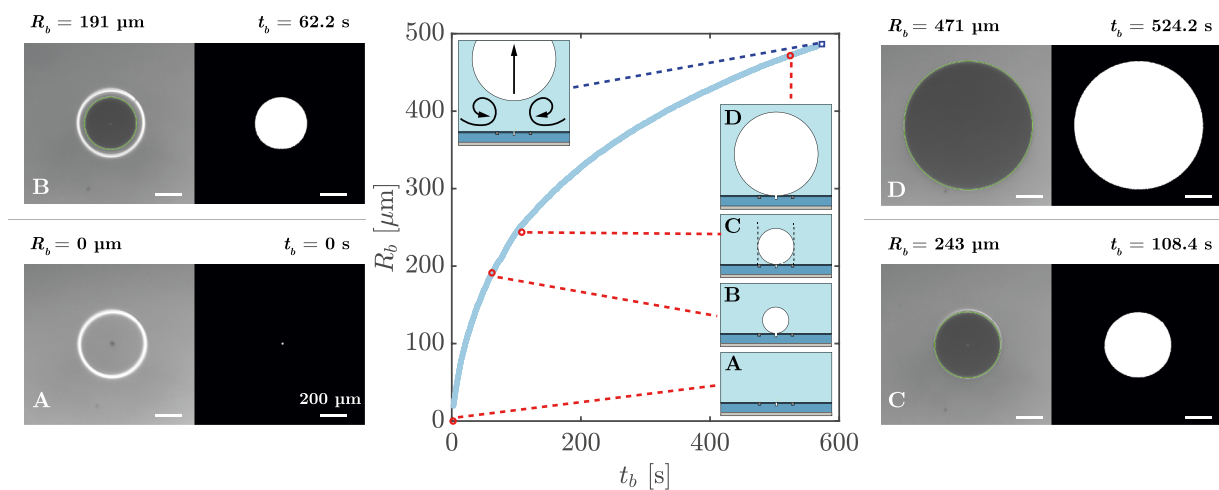

Fig. 2. Bubble radius R_b plotted against bubble lifetime t_b for one bubble driven by a constant current of 10 µA. The experimental (top-view) image (left) paired with its binarized counterpart (right) is shown for four distinct frames. In frame A, there is no bubble and the small dark region at the centre of the ring corresponds to the hydrophobic pit. The platinum ring electrode is clearly visible as a white ring in frames A and B, whereas it is largely covered by the bubble in C. All scale bars correspond to 200 µm. The circular bubble contour detected by the algorithm is shown in green. The values of R_b for frames A–D are indicated by the red circle markers. Representative experimental movies are available as supplementary information SI2 and SI3.
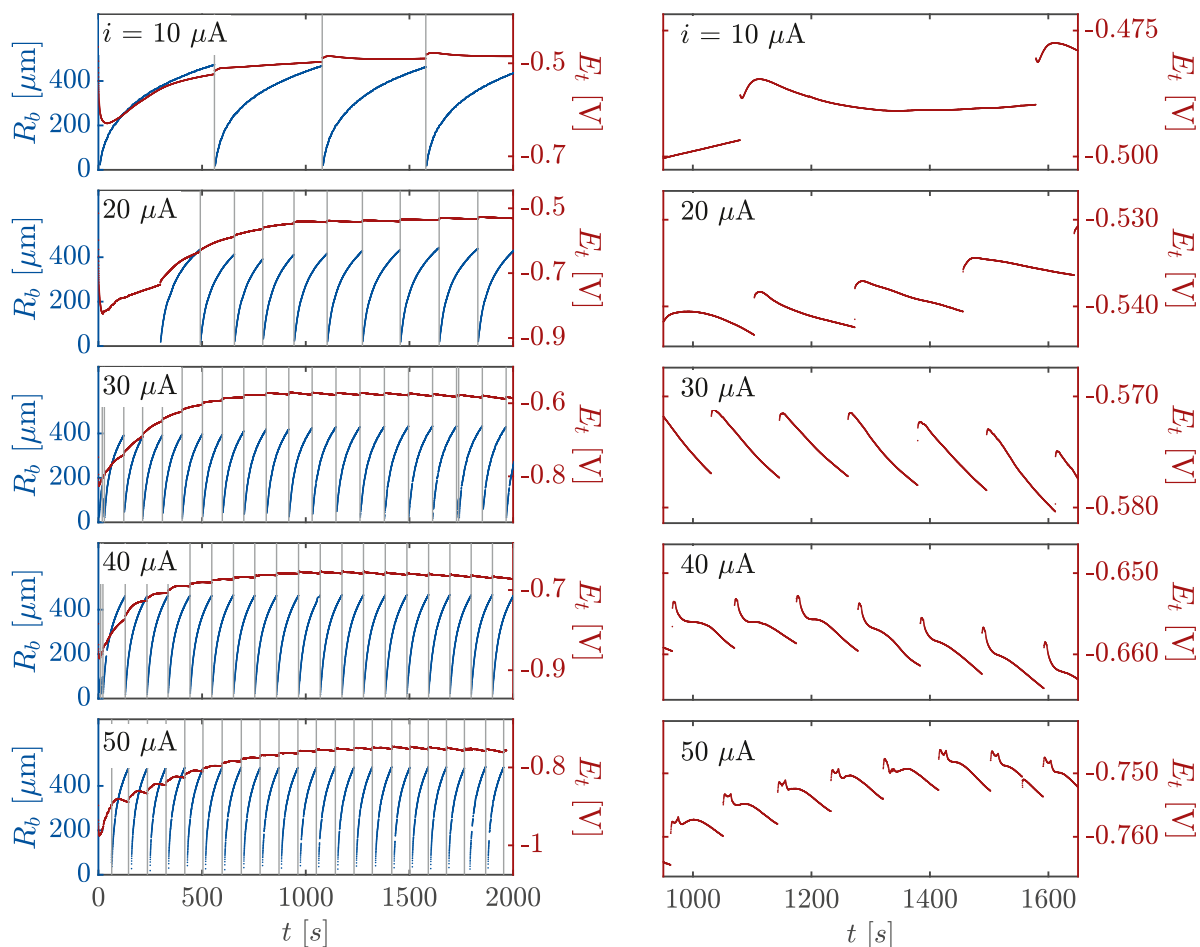
Fig. 3. Left-column panels: bubble radius R_b and half-cell potential E_t (vs. RHE) plotted against time t since the start of electrolysis for five different applied currents. The data are shown for $t < 2000$ s. Right-column panels: Zoom-ins of the half-cell potential curves.

be discussed in detail in Section 3.3. Finally, we comment on the fact that the base magnitude of E_t drops by approximately 0.2 V from an initial value to the steady-state value over the course of approximately 1000 s (see Fig. 3, left panels). Note that this drop is ~ 20 times larger than the fluctuations caused by the growth and departure of bubbles (which are of the order of ~ 0.01 V) and occurs across a timescale several times the lifetime of a bubble (~ 4 times the lifetime of a bubble at 10 µA and ~ 20 times the lifetime of a bubble at 50 µA). The magnitude and relaxation time of this drop are largely independent of the applied current. The drop can be attributed to the diffuse charge dynamics of the electrochemical system: namely, to the double-layer charging and bulk ionic diffusion (or rather migration) within the electrolyte towards an equilibrium distribution. In fact, the relaxation time observed here is closer to the expected timescale of ionic bulk diffusion $\tau_L = L^2/D_i \sim 10^3$ s, (taking $2L \sim 3$ mm as the inter-electrode distance and $D_i \sim 10^{-9}$ m²/s as the ionic diffusivity) than to the much shorter Debye charging time, which is typically in the order of 10^{-9} s to 10^{-6} s for aqueous systems [62]. Note that the nucleation, growth and departure of bubbles influences the development of the concentration profile. This explains the shorter timescale (~ 300 s) observed by Pande et al. who monitored the development of the ph profiles using confocal fluorescence microscopy at low current densities (< 100 µA/cm²) in the absence of bubbles [63].

3.1. Bubble growth

The effect of current density on the bubble growth rate is well seen in Fig. 4(a), which plots R_b as a function of the bubble lifetime t_b for a total

of 332 bubbles (belonging to 25 different successions) generated at different applied currents. For every current, the small thickness of the envelope comprising the corresponding population of $R_b(t_b)$ curves demonstrates reasonable reproducibility across experiments. In fact, the bubble growth rate was found to be largely proportional to the current density. As seen in Fig. 4(b), the growth curves nearly collapse into a single curve when plotting R_b as a function of charge it_b, or rather $n_{H_2} = it_b/2F$, the number of moles of hydrogen evolved at the electrode. However, $R_b(n_{H_2})$ grows noticeably faster for the highest currents than for the lowest ones. This clearly indicates that the proportion of evolved hydrogen gas absorbed by the bubble improves with increasing current. The gas-evolution efficiency of the system will be discussed further in the next subsection. Despite the i-dependence of the gas evolution efficiency, the nature of the growth dynamics remains similar for all currents. The double logarithmic plot of $R_b(n_{H_2})$ in Fig. 4(c) reveals that our bubbles cannot be described by a single power-law of the form $R_b \sim t_b^\alpha$. Instead, $R_b(t_b)$ follows a continuous transition from pressure-driven growth ($\alpha = 1$) towards reaction-limited growth ($\alpha = 1/3$). This agrees with previous reports where bubbles likewise did not adhere to any particular regime throughout the entire growth process [29]. The bubble radius R_b in Fig. 4(c) has been normalised by $R_e = 242.5$ µm, the mean radius of the ring electrode encircling the base of the bubble, in order to highlight the fact that the change in slope is sharpest once the bubble outgrows the electrode, i.e., when $R_b/R_e \approx 1$. The corresponding transition of the local time exponent $\alpha(t)$ is verified in Fig. 4(d), noting that α is equivalent to the local logarithmic slope of the curves in Fig. 4 (d), namely $\alpha = \mathrm{d}\ln(R_b/R_e)/\mathrm{d}\ln(n_{H_2})$. The local logarithmic slope is obtained by fitting a smoothing spline to the curves in Fig. 4(c) and then
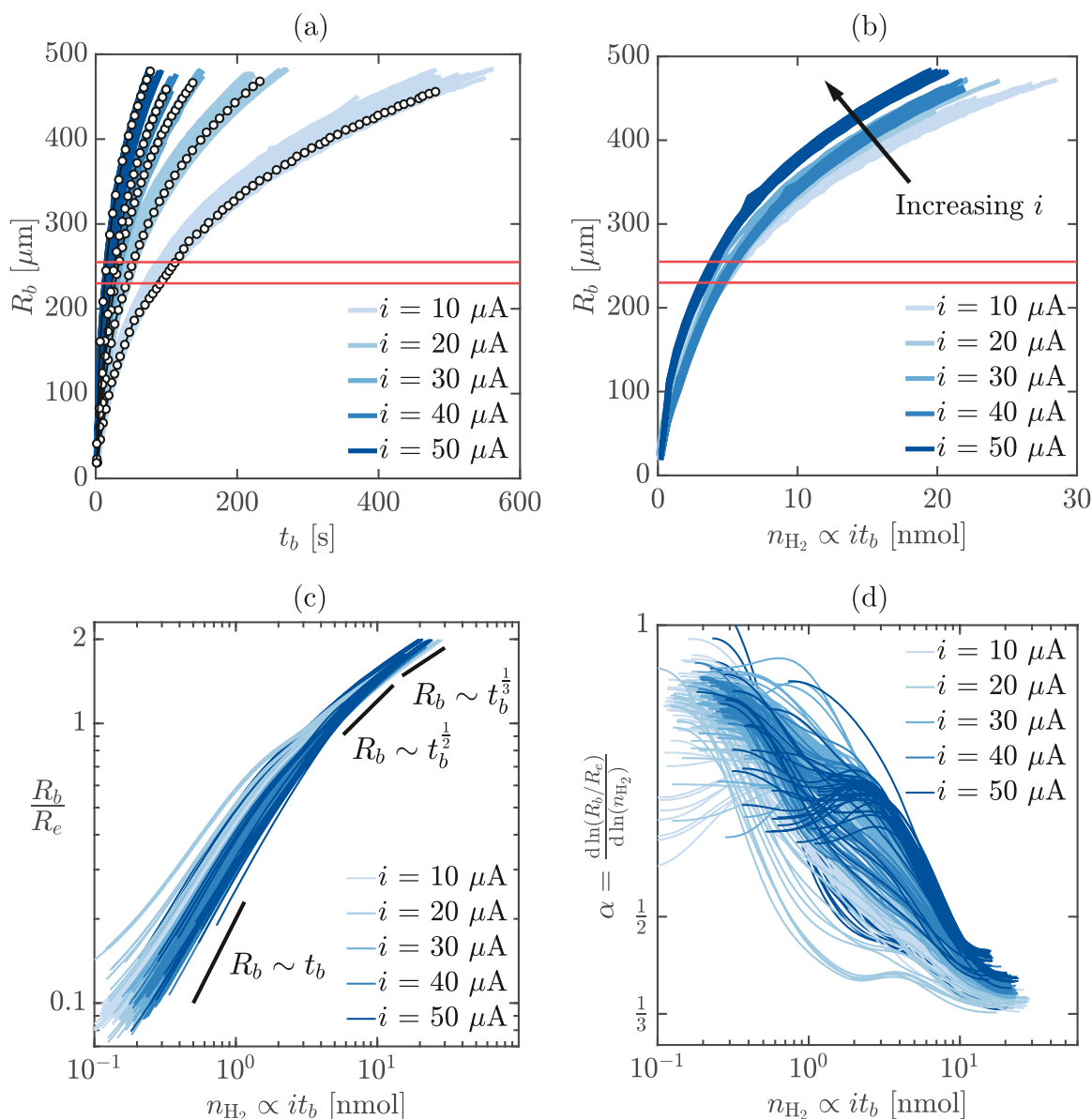
Fig. 4. (a) Bubble radius R_b as a function of t_b, the time during the lifetime of each bubble, for a total of 332 bubbles belonging to 25 different experiments (bubble successions) at five different currents i (see legend). The growth curves are colour-coded with the applied current. For each current, the growth curve of one particular bubble is highlighted (white circles) for reference. The horizontal red lines indicate the inner and outer radii of the ring electrode. (b) Bubble radius versus the moles of hydrogen evolved at the electrode n_{H_2}, which is proportional to the amount of charge transferred at the electrode. In (b), for clarity only one experiment per current is plotted. (c) Logarithmic plot of the bubble radius (normalised by the mean radius R_e of the ring electrode) versus the moles of hydrogen evolved at the electrode, n_{H_2}. A total of 332 growth curves from 25 different experiments are plotted. (d) The local logarithmic slope α of the curves in (c) plotted against n_{H_2}, where α represents the local time exponent assuming that $R_b \propto t_b^\alpha$ at any given time. Regardless of the current, the bubble growth dynamics follows a continuous transition from pressure-driven growth ($\alpha \sim 1$) towards reaction-limited growth ($\alpha = 1/3$).

calculating the numerical derivative. The low camera framerate limits the accuracy of fits in the region $n_{H_2} < 10^0$ nmol in 4(d). Thus, a simplistic interpretation of the growth dynamics is that the bubble exhibits effectively a short pressure-driven growth phase (when $R_b/R_e \ll 1$, $\alpha = 1$), followed by a smooth transition which spans a second phase where diffusion-limited growth is presumably dominant (up to $R_b/R_e \approx 1$, $\alpha = 1/2$) and tends towards a third phase primarily driven by supply-limited (reaction-limited) growth (when $R_b/R_e > 1$, $\alpha = 1/3$).

3.2. Gas-evolution efficiency

The gas-evolution efficiency is commonly defined as the ratio between the amount of gas present in a departing bubble and the amount of gas produced by the electrode during the lifetime of the bubble [27,

64]. The fact that the gas-evolution efficiency of our system improves with current density (cf. Fig. 4b) can be explained with regards to a differential form of the efficiency which provides insight into the mass transfer within the lifetime of a single bubble. The instantaneous gas-evolution efficiency η is thus defined as the ratio of the molar accumulation rate of H_2 into the growing bubble and the molar production rate of H_2 at the electrode:

$$\eta = \frac{dn_b/dt_b}{dn_{H_2}/dt_b} = \frac{4\pi P_0/3\mathcal{R}T_0}{i/2F}\frac{dR_b^3}{dt_b} = \frac{4\pi P_0/\mathcal{R}T_0}{i/2F}R_b^2\frac{dR_b}{dt_b}, \qquad (3)$$

where n_b is the number of moles of H_2 gas in the bubble, P_0 the ambient pressure and T_0 the ambient temperature. The Laplace pressure in the bubble is neglected because $2\sigma/R_b \ll P_0$ for the majority of the lifetime
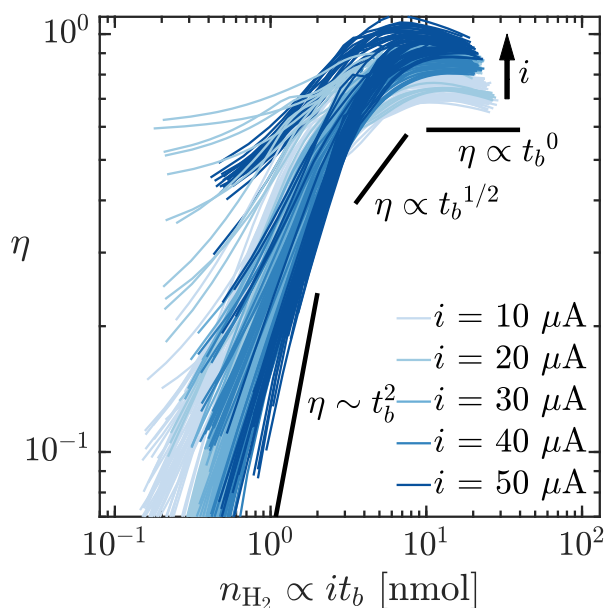
Fig. 5. Instantaneous gas-evolution efficiency η of individual bubbles versus moles of hydrogen evolved at the electrode (for a total of 332 bubbles driven at one of the five currents considered). The efficiency increases in time (transitioning across the pressure-driven and diffusion-limited growth stages) and eventually plateaus (indicative of supply-limited growth).

of the bubbles, with $\sigma = 72 \times 10^{-3}$ N/m the interfacial surface tension of hydrogen in water (see SI1 Section S2). In Fig. 5, η is calculated by smoothing R_b vs. t_b data with robust locally weighted regression filter [65] using a second order polynomial and then calculating the gradient using the central difference method. The assumption that $R_b \propto t_b^{\alpha}$ implies that $\eta \propto t_b^{3\alpha-1}$. The previously discussed regimes for $\alpha = 1, 1/2$ and $1/3$ thus correspond to $\eta \propto t_b^2$ (pressure-driven), $\eta \propto t_b^{1/2}$ (diffusion-limited) and $\eta \propto t_b^0$ (supply- or reaction-limited), respectively. These are marked in Fig. 5, which reveals that η is always lowest at the start of bubble growth. The efficiency increases in time and eventually plateaus, as expected for supply-limited growth. The latter is usually encountered when the bubble takes up nearly all of the gas generated at the electrode, i.e., when $\eta \approx 1$ [31,32]. While this is the case for the highest current (where $\eta \sim 90$ %), η always remains reasonably constant in time even for the lowest currents, albeit at $\eta \sim 60$ %. A possible explanation is that once $R_b > R_e$, the bubble absorbs most of the hydrogen gas generated by the ring electrode underneath but simultaneously expels some gas from its apex to the locally-undersaturated bulk electrolyte. This equilibrium between uptake and loss to the surroundings results in a fairly constant but non-unity η. Increasing the current density implies that the bubble grows faster and loses less H_2 to the bulk of the electrolyte, thus resulting in a higher η. In fact, bubble departure times are $\approx 35\,\tau_d$ at 10 µA while only $\approx 5\,\tau_d$ at 50 µA, where $\tau_d = R_e^2/D \approx 13$ s denotes the characteristic diffusion timescale for our system based on $D = 4.5 \times 10^{-9}$ m^2/s, the diffusivity of hydrogen in water.

3.3. Total overpotential

The nature of the periodic fluctuations of the total overpotential (cf. Fig. 3, right panels) can be associated to the competition between several constituent phenomena present during the bubble lifetime. Their impact on E_t can be better understood by splitting the latter into three components [41]:

$$E_t = \overline{E}_a + E_\Omega + E_c. \tag{4}$$

Component $\overline{E}_a$ refers to the unperturbed activation or surface over-

potential of the ring electrode. It arises from the finite kinetics of the cathodic reaction in the absence of product gas supersaturation or concentration polarization of the reacting ions. Note that $\overline{E}_a$ is a spatially-averaged quantity to accommodate for a non-uniform current density distribution; hence $\overline{E}_a$ is purely a function of the applied current i.

The Ohmic overpotential E_Ω mainly represents the loss due to the solution resistance between the working and the reference electrode. In our case, hyperpolarization is negligible—the constant-current condition and zero bubble coverage preclude any significant magnification or distortion or the current density distribution on the working electrode. Note that additional Ohmic losses due to the external circuit are not considered. This is justified since we focus on changes in overpotential components and do not derive our results from their absolute magnitudes. Ohmic losses due to external connections are constant and any fluctuations in the half-cell potential can be attributed to the bubbles.

Lastly, the concentration overpotential E_c is associated with the influence of the oversaturation of ionic and dissolved H_2 molecules on the cathode reaction kinetics. Given the relatively high electrolyte concentration, variations in E_c (in the time scale of the bubble lifetime) are expected to arise from fluctuations in the H_2 concentration alone. In our system, (i) continuous Faradaic production of H_2 results in the accumulation of dissolved gas and E_c increases in magnitude. On the other hand, (ii) the transport of dissolved H_2 by diffusion and convection lower the local concentration of dissolved gas and hence reduce $|E_c|$. Convective flows may arise from density-driven natural convection sustained by prominent concentration or thermal gradients in the vicinity of the electrode [66,67], as well as from solutal or thermal Marangoni convective flows (i.e., driven by gradients in the surface tension), which are strongest in the liquid wedge between the base of the bubble and the electrode [68–75]. Additionally, the growing bubble acts as a sink for the dissolved gas produced at the electrode surface which also lowers $|E_c|$. This is referred to as (iii) the concentration-lowering effect (CLE). On the other hand, the insulating bubble surface constricts the passage of current to the electrode (see Fig. 7(a) for schematic). This is referred to as (iv) the shielding effect (SE). It results in an increase of the solution resistance and hence in $|E_\Omega|$. Both CLE and SE increase with $R_b(t)$. Lastly, (v) bubble detachment provokes an instantaneous drop in $|E_t|$. The electrode is no longer shielded and the Ohmic loss is instantaneously relieved, i.e., the passage of current is no longer constrained by the bubble surface (the system reverts from resembling schematic 3 on Fig. 7(a) to schematic 1). Furthermore, the advected electrolyte in the bubble wake disrupts the concentration field of H_2 previously established near the electrode. The different contributions of these phenomena (i–v) in time can be illustrated with reference to Fig. 6, which correlates $E_t(t)$ with $R_b(t)$ during the life time of a single bubble for different currents. Note that the cycles for subsequent bubbles are practically identical. We identify three stages in the evolution of E_t. Initially, there is a short *incipient stage* [green regions in Fig. 6(a–f)]. Following the detachment-induced drop, E_t remains largely constant. Any notable gas build-up at the electrode is precluded by the lack of a measurable delay between one bubble departing and the next bubble nucleating, in addition to the disruptive flow of electrolyte induced by the preceding bubble. The end of the convective stage is marked by an extremum in overpotential ($dE_t/dt_b = 0$), as delimited by the first vertical line in Figs. 6(a–f). Subsequently, there is a *mixed stage* (yellow regions). Several phenomena compete in this stage and the dominant effect strongly depends on the current applied. For $i = 10$ µA [see Fig. 6(a, d)] we observe that $|E_t|$ decreases after the inflection. At such a low applied current, CLE and gas transport to the bulk are able to overcome the buildup of H_2 concentration until the shielding effect becomes significant towards the end of the stage. At 30 µA [Fig. 6(b, e)], the larger rate of gas production at the electrode balances CLE and the transport of H_2 to the electrolyte. At 50 µA [Fig. 6(c, f)], gas-build up from Faradaic gas production overcomes diffusion to the bulk and CLE, resulting in an
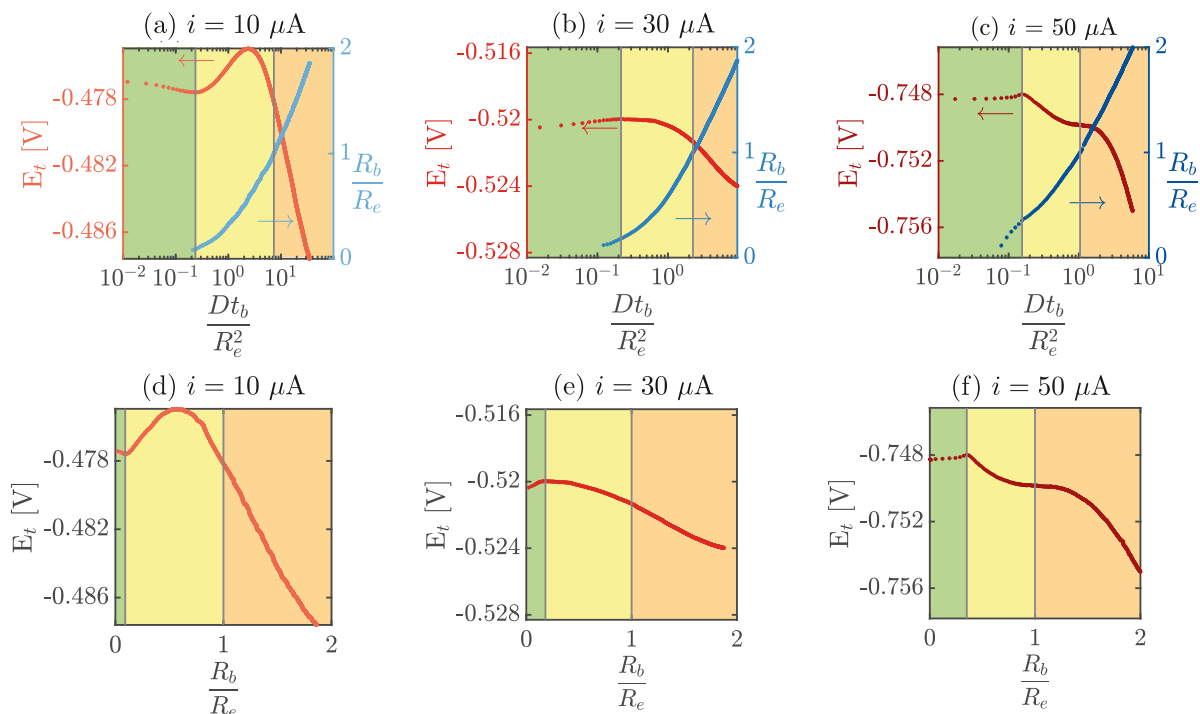
Fig. 6. (a–c) Total overpotential E_t (red points) and dimensionless radius R_b/R_e (blue points) plotted as functions of dimensionless time Dt_b/R_e^2 for one typical bubble at different applied currents on a linear–log scale. (d–f) E_t vs. dimensionless radius R_b/R_e corresponding to the same bubbles considered in the plots (a–c) above. The scale bar of E_t is kept constant across the plots to enable a comparison of the magnitude of the fluctuations at different currents. The two vertical lines divide the plots into three distinct regions termed incipient stage (green region), mixed stage (yellow), and shielding stage (orange), where changes in E_t are dominated by different effects (main text). (For interpretation of the references to color in this figure legend, the reader is referred to the web version of this article.)

increase in $|E_t|$. The mixed stage ends when R_b becomes comparable to the electrode size, i.e., at $R_b/R_e = 1$, as delimited by the second vertical line in Fig. 6(a–f). Interestingly, the temporary balance in E_t observed between at the very end of the mixed stage in Fig. 6(c, f) can be attributed to the fact that CLE also increases with R_b. Finally, for $R_b/R_e > 1$ there is a *shielding stage* (orange regions). The shielding effect is now dominant given that the bubble eclipses the electrode ring beneath, which results in the monotonic increase of $|E_t|$ in time regardless of the current. The CLE and transport of H_2 to the bulk are thus overcome by SE and Faradaic gas production. Notably, the rate of increase of $|E_t|$ does not increase with increasing i. This is explained by the fact that the rate of increase in the CLE is also dependent on the current as explained in the next section.

3.4. Effect of bubble size in the overpotential components

The transport of dissolved gas away from the electrode is often influenced by physicochemical hydrodynamics such as density-driven and Marangoni flows [72]. For this reason, fluctuations arising from the concentration overpotential component E_c are difficult to estimate, let alone accurately model. In our case, however, the impact of the bubble size R_b on the Ohmic component (E_Ω) can be straightforwardly estimated under the assumption of uniform ionic concentration in the electrolyte, by virtue of the relatively high electrolyte concentration employed in the experiments. It follows that the electric field in the electrolyte is time-independent and obeys Ohm's law, with $\kappa = 0.735$ S/m as the measured conductivity of the electrolyte. The electric field was numerically solved using COMSOL Multiphysics on a 3D domain that closely resembles the experimental cell with the appropriate set of boundary conditions (see SI1, Section S5 for the mathematical formulation and the geometry of the numerical domain). The bubble boundary is prescribed as a stationary sphere of constant radius R_b. The ring-electrode kinetics are modelled by the Tafel equation; the exchange

current density and Tafel slope were obtained from cyclic voltammetry (see SI1, Section S4). In the steady-state simulations performed, the bubble size was systematically varied within $0 < R_b/R_e < 2$ for $i = 10$, 20, 30, 40 and 50 μA. Hyperpolarization was found to be indeed negligible—the axisymmetric current density profile on the ring surface was always found to vary within just 2% of the mean value. Therefore, the Ohmic loss E_Ω arises precisely from the uncompensated potential drop, namely, the (average) difference in electrolyte potential from the ring electrode to the reference electrode [76]. Consequently, according to Ohm's law, E_Ω scales as

$$i/R_e^2 \sim \kappa|E_\Omega|/L, \tag{5}$$

where $L = 2.4$ mm is the inter-electrode distance. To quantify the effect of R_b on E_Ω, we consider the change in E_Ω in the presence of a bubble of size R_b with respect to a scenario with no bubble, i.e., $\Delta E_\Omega(R_b) \equiv E_\Omega(R_b) - E_\Omega(0)$. The change in the Ohmic overpotential ΔE_Ω according to the simulations is plotted in dimensionless form in the inset of Fig. 7 (b) as a function of R_b for all five currents. Ohm's law [Eq. (5)] explains why the curves of dimensionless overpotential, $\Delta E_\Omega/i\kappa^{-1}l^{-1}$, with $l = R_e^2/L$ as the characteristic length, collapse onto the same curve for all i. The passage of current is constrained to a narrow wedge of electrolyte between the substrate at bottom and the insulating surface of the bubble (see Fig. 7(a)). The wedge of electrolyte between the bubble and the substrate grows smaller as the bubble grows larger. Therefore, E_Ω grows at an increasing rate with R_b, as a consequence of the stronger shielding effect by the bubble. This result is consistent with the behavior of $E_t(t)$ during the shielding stage in Fig. 6. It should be pointed out that the magnitude of ΔE_Ω obtained from simulations is comparable to the experimental fluctuations of the total overpotential ($\Delta E_\Omega \sim \Delta E_t \sim 0.01$ V); however, the absolute magnitudes are not: $|E_\Omega| \sim 0.01$ V whereas $|E_t| \sim 1$ V. The activation overpotential $\bar{E}_a$ accounts for the majority of the latter.
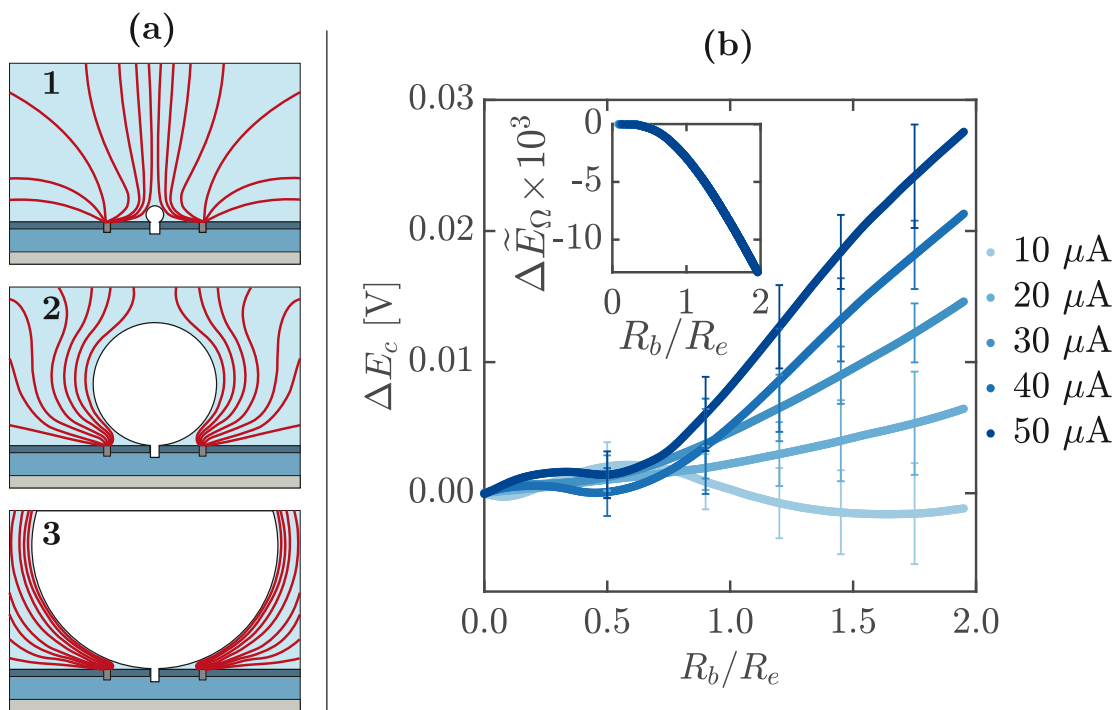
Fig. 7. (a) Schematic representation of current density lines (red) around the bubble. As the bubble grows, flux lines are confined to a narrow wedge of electrolyte between the bubble surface and the substrate and the Ohmic overpotential increases as a result. This increased Ohmic loss is instantaneously relieved upon departure because flux lines are no longer constricted (the system reverts from 3 to 1). (b) Inset: change of the dimensionless Ohmic overpotential $\Delta \widetilde{E}_\Omega \equiv \kappa l \Delta E_\Omega / i$ according to the simulations as a function of the normalised bubble radius. All five currents collapse onto the same curve. The negative change implies an increase of the (negative) Ohmic overpotential. Main: change of the concentration overpotential ΔE_c versus bubble size for all five currents. ΔE_c is calculated by subtracting ΔE_Ω (simulations) from the (average) change in total overpotential ΔE_t obtained from the experiments. The error bars represent two standard deviations about the mean. A positive ΔE_c implies a reduction of the (negative) concentration overpotential.

Finally, the effect of R_b on the concentration overpotential component can be estimated from the simulated ΔE_Ω (using that $\overline{E}_a$ is independent of the presence of the bubble) as

$$\Delta E_c = \Delta E_t - \Delta E_\Omega, \tag{6}$$

where ΔE_t refers to the corresponding change of the half-cell (total) overpotential, averaged over the total number of bubbles analysed at each current.

Notably, the concentration lowering effect is weak and in fact ΔE_c turns negative for bubbles driven by an electrolysis current of 10 μA. As seen in Fig. 5, the maximum η exhibited by bubbles driven by 10 μA is $\sim$ 0.6. This indicates that $\sim$ 40% of all the hydrogen produced during the lifetime of a bubble, diffuses into the electrolyte in the vicinity of the electrode. This raises the concentration of dissolved hydrogen and leads to an increase in $|E_c|$ (i.e. $\Delta E_c < 0$). For all currents greater than 10 μA, Fig. 7(b) reveals that the bubble diminishes $|E_c|$ indeed ($\Delta E_c > 0$). The concentration-lowering effect becomes notable for $R_b / R_e > 1$ and increases (in magnitude) with increasing R_b and also with increasing i. The latter is compatible with the observation that the gas-evolution efficiency η also improves with i in the reaction-limited growth stage of the bubble (see Fig. 5). This indicates that CLE increases with increasing η.

However, the result that the CLE strengthens with R_b for $R_b / R_e > 1$ might seem to contradict the fact that η plateaus in time—η thus remains R_b-invariant—during the same time period. One plausible explanation is the gradual inducement of stronger convection as the bubble grows larger [77–79], which enhances the transport of H_2 away from the electrode surface, but not necessarily into the bubble itself. The second explanation resorts to the aforementioned hypothesis discussed in Section 3.2. Namely, that the gas uptake flux (hence CLE) and loss flux experienced by the bubble must both increase at comparable rates during bubble growth, which would then result in η remaining

effectively constant over time.

4. Conclusions and outlook

We have investigated the growth of successive hydrogen bubbles generated by constant-current alkaline water electrolysis and their impact on the half-cell overpotential in the absence of hyperpolarization, i.e., with zero surface bubble coverage. The bubble nucleation site is decoupled from the electrode surface, as the bubbles nucleate from a hydrophobic cavity encircled by a thin Pt ring electrode embedded in a microfabricated Si substrate. First, we show that under these conditions, the dynamics of bubble growth does not adhere to one particular scaling law in time, but undergoes a smooth transition from pressure-driven growth towards reaction-limited (supply-limited) growth. This is also reflected in the instantaneous gas-evolution efficiency, which plateaus once the radius of the bubble outgrows that of the ring electrode. The efficiency increases with the applied current. The rich behaviour of the half-cell overpotential during the lifetime of the bubble results from the interplay between several (bubble-induced) phenomena including gas absorption, Ohmic shielding and detachment-induced convection. The overpotential exhibits a strong dependence on the stage of bubble growth and the applied current. Nonetheless, the overpotential eventually always increases once the bubble outgrows the ring electrode. This is a consequence of the dominant effect of Ohmic shielding, namely, the increase in potential drop across the constricted electrolyte. Finally, the increasing effect of bubble size on the Ohmic component of the overpotential was quantified numerically by means of a steady-state model, which in turn allowed for the influence of bubble size on the concentration overpotential component to be estimated. It is found that the bubble induces a lowering effect on the concentration overpotential which strengthens with both increasing bubble size and increasing applied current. Future challenges along the current path

towards optimal bubble management comprise the design of next-generation, bubble-free electrodes, which are able to skew the competition between the bubble-induced Ohmic loss and the concentration-lowering effect in favour of the latter. Our findings, so far applicable to single bubble generation, also warrant further research into more complex electrolytic systems consisting of, e.g., a group of bubbles growing on an ordered array of (ring) microelectrodes. Here, collective effects and interactions between neighbouring bubbles, such Ostwald ripening/shielding, bubble coalescence and large-scale convective patterns, are expected to play a crucial role in the resulting overpotential response and the net efficiency of mass transfer.

CRediT authorship contribution statement

Akash Raman: Conceptualization, Data curation, Formal analysis, Investigation, Methodology, Software, Visualization, Writing – original draft, Writing – review & editing. **Pablo Peñas:** Conceptualization, Data curation, Formal analysis, Investigation, Methodology, Software, Visualization, Writing – original draft, Writing – review & editing. **Devaraj van der Meer:** Funding acquisition, Methodology, Supervision, Writing – review & editing. **Detlef Lohse:** Funding acquisition, Methodology, Supervision, Writing – review & editing. **Han Gardeniers:** Funding acquisition, Project administration, Supervision, Writing – review & editing. **David Fernández Rivas:** Funding acquisition, Project administration, Resources, Supervision, Writing – review & editing.

Declaration of Competing Interest

The authors declare that they have no known competing financial interests or personal relationships that could have appeared to influence the work reported in this paper.

Acknowledgements

Supplementary material

Supplementary material associated with this article can be found, in the online version, at doi:10.1016/j.electacta.2022.140691

References

[1] Z.J. Schiffer, K. Manthiram, Electrification and decarbonization of the chemical industry, Joule 1 (1) (2017) 10–14, https://doi.org/10.1016/j.joule.2017.07.008.

[2] R.S. Weber, Effective use of renewable electricity for making renewable fuels and chemicals, ACS Catal. 9 (2) (2019) 946–950, https://doi.org/10.1021/acscatal.8b04143.

[3] L.D. Ellis, A.F. Badel, M.L. Chiang, R.J.-Y. Park, Y.-M. Chiang, Toward electrochemical synthesis of cement–an electrolyzer-based process for decarbonating CaCO3 while producing useful gas streams, Proc. Natl. Acad. Sci. USA 117 (23) (2020) 12584–12591, https://doi.org/10.1073/pnas.1821673116.

[4] D.E. Blanco, M.A. Modestino, Organic electrosynthesis for sustainable chemical manufacturing, Trends Chem. 1 (1) (2019) 8–10, https://doi.org/10.1016/j.trechm.2019.01.001.

[5] I. Garagounis, A. Vourros, D. Stoukides, D. Dasopoulos, M. Stoukides, Electrochemical synthesis of ammonia: recent efforts and future outlook, Membranes 9 (9) (2019) 112.

[6] S. Agarwal A, Y. Zhai, D. Hill, N. Sridhar, The electrochemical reduction of carbon dioxide to formate/formic acid: engineering and economic feasibility,

[7] M.C. Leech, K. Lam, Electrosynthesis using carboxylic acid derivatives: new tricks for old reactions, Acc. Chem. Res. 53 (1) (2020) 121–134, https://doi.org/10.1021/acs.accounts.9b00586.

[8] S. Mena, S. Santiago, I. Gallardo, G. Guirado, Sustainable and efficient electrosynthesis of naproxen using carbon dioxide and ionic liquids, Chemosphere 245 (2020) 125557, https://doi.org/10.1016/j.chemosphere.2019.125557.

[9] P. Moriarty, D. Honnery, Intermittent renewable energy: the only future source of hydrogen? J. Hydrogen Energy 32 (12) (2007) 1616–1624, https://doi.org/10.1016/j.ijhydene.2006.12.008.

[10] B.R. Alamri, A.R. Alamri, Technical review of energy storage technologies when integrated with intermittent renewable energy. 2009 International Conference on Sustainable Power Generation and Supply, 2009, pp. 1–5, https://doi.org/10.1109/supergen.2009.5348055.

[11] L.M. Pierpoint, Harnessing electricity storage for systems with intermittent sources of power: policy and R&D needs, Energy Policy 96 (2016) 751–757, https://doi.org/10.1016/j.enpol.2016.04.032.

[12] D. Zhang, K. Zeng, Evaluating the behavior of electrolytic gas bubbles and their effect on the cell voltage in alkaline water electrolysis, Ind. Eng. Chem. Res. 51 (42) (2012) 13825–13832, https://doi.org/10.1021/ie301029e.

[13] S.M. H. Hashemi, M.A. Modestino, D. Psaltis, A membrane-less electrolyzer for hydrogen production across the pH scale, Energy Environ. Sci. 8 (7) (2015) 2003–2009, https://doi.org/10.1039/C5EE00083A.

[14] S.M.H. Hashemi, P. Karnakov, P. Hadikhani, E. Chinello, S. Litvinov, C. Moser, P. Koumoutsakos, D. Psaltis, A versatile and membrane-less electrochemical reactor for the electrolysis of water and brine, Energy Environ. Sci. 12 (5) (2019) 1592–1604, https://doi.org/10.1039/C9EE00219G.

[15] J.M. Chin Kwie Joe, L.J.J. Janssen, S.J.D. van Strelen, J.H.G. Verbunt, W. M. Sluyter, Bubble parameters and efficiency of gas bubble evolution for a chlorine-, a hydrogen- and an oxygen-evolving wire electrode, Electrochim. Acta 33 (6) (1988) 769–779, https://doi.org/10.1016/S0013-4686(98)80006-6.

[16] M. Alam, W. Yang, K. Mohanarangam, G. Brooks, Y.S. Morsi, Investigation of anodic gas film behavior in Hall–Heroult cell using low temperature electrolyte, Metall. Mater. Trans. B 44 (5) (2013) 1155–1165, https://doi.org/10.1007/s11663-013-9885-x.

[17] A. Cubeddu, V. Nandana, U. Janoske, A numerical study of gas production and bubble dynamics in a Hall-Héroult reduction cell, in: C. Chesonis (Ed.), Light Metals 2019, The Minerals, Metals & Materials Series, Springer International Publishing, Cham, 2019, pp. 605–613, https://doi.org/10.1007/978-3-030-05864-7_75.

[18] A.L. Perron, L.I. Kiss, S. Poncsák, Mathematical model to evaluate the Ohmic resistance caused by the presence of a large number of bubbles in Hall-Héroult cells, J. Appl. Electrochem. 37 (3) (2007) 303–310, https://doi.org/10.1007/s10800-006-9219-7.

[19] J. St-Pierre, A.A. Wragg, Behaviour of electrogenerated hydrogen and oxygen bubbles in narrow gap cells—part II. Application in chlorine production, Electrochim. Acta 38 (13) (1993) 1705–1710, https://doi.org/10.1016/0013-4686(93)85065-7.

[20] A. Angulo, P. van der Linde, H. Gardeniers, M. Modestino, D. Fernández Rivas, Influence of bubbles on the energy conversion efficiency of electrochemical reactors, Joule 4 (3) (2020) 555–579, https://doi.org/10.1016/j.joule.2020.01.005.

[21] G.F. Swiegers, A.L. Hoang, A. Hodges, G. Tsekouras, C.-Y. Lee, K. Wagner, G. Wallace, Current status of membraneless water electrolysis cells, Curr. Opin. Electrochem. 32 (2022) 100881, https://doi.org/10.1016/j.coelec.2021.100881.

[22] O.R. Enríquez, C. Hummelink, G.-W. Bruggert, D. Lohse, A. Prosperetti, D. van der Meer, C. Sun, Growing bubbles in a slightly supersaturated liquid solution, Rev. Sci. Instrum. 84 (6) (2013) 065111, https://doi.org/10.1063/1.4810852.

[23] Á. Moreno Soto, S.R. German, H. Ren, D. van der Meer, D. Lohse, M.A. Edwards, H. S. White, The nucleation rate of single O2nanobubbles at Pt nanoelectrodes, Langmuir 34 (25) (2018) 7309–7318.doi:3

[24] S.R. German, M.A. Edwards, Q. Chen, Y. Liu, L. Luo, H.S. White, Electrochemistry of single nanobubbles. Estimating the critical size of bubble-forming nuclei for gas-evolving electrode reactions, Faraday Discuss. 193 (0) (2016) 223–240, https://doi.org/10.1039/C6FD00099A.

[25] S.R. German, M.A. Edwards, H. Ren, H.S. White, Critical nuclei size, rate, and activation energy of H2 gas nucleation, J. Am. Chem. Soc. 140 (11) (2018) 4047–4053, https://doi.org/10.1021/jacs.7b13457.

[26] D.E. Westerheide, J.W. Westwater, Isothermal growth of hydrogen bubbles during electrolysis, AIChE J. 7 (3) (1961) 357–362, https://doi.org/10.1002/aic.690070303.

[27] P. van der Linde, A. Moreno Soto, P. Peñas-López, J. Rodríguez-Rodríguez, D. Lohse, H. Gardeniers, D. van der Meer, D. Fernández Rivas, Electrolysis-driven and pressure-controlled diffusive growth of successive bubbles on microstructured surfaces, Langmuir 33 (45) (2017) 12873–12886, https://doi.org/10.1021/acs.langmuir.7b02978.

[28] S.J.D. van Stralen, W.M. Sluyter, Mass diffusion-controlled bubble behaviour in boiling and electrolysis and effect of bubbles on Ohmic resistance, J. Appl. Electrochem. 15 (4) (1985) 527–536, https://doi.org/10.1007/BF01059294.

[29] N.P. Brandon, G.H. Kelsall, Growth kinetics of bubbles electrogenerated at microelectrodes, J. Appl. Electrochem. 15 (4) (1985) 475–484, https://doi.org/10.1007/BF01059288.

[30] J.P. Glas, J.W. Westwater, Measurements of the growth of electrolytic bubbles, Int. J. Heat Mass Transf. 7 (12) (1964) 1427–1443, https://doi.org/10.1016/0017-9310(64)90130-9.

ChemSusChem 4 (9) (2011) 1301–1310, https://doi.org/10.1002/cssc.201100220.

[31] X. Yang, F. Karnbach, M. Uhlemann, S. Odenbach, K. Eckert, Dynamics of single hydrogen bubbles at a platinum microelectrode, Langmuir 31 (29) (2015) 8184–8193, https://doi.org/10.1021/acs.langmuir.5b01825.

[32] D. Fernández, P. Maurer, M. Martine, J.M.D. Coey, M.E. Möbius, Bubble formation at a gas-evolving microelectrode, Langmuir 30 (43) (2014) 13065–13074, https://doi.org/10.1021/la500234r.

[33] R. Darby, M.S. Haque, The dynamics of electrolytic hydrogen bubble evolution, Chem. Eng. Sci. 28 (5) (1973) 1129–1138, https://doi.org/10.1016/0009-2509(73)85022-5.

[34] H.F.A. Verhaart, R.M. de Jonge, S.J.D. van Stralen, Growth rate of a gas bubble during electrolysis in supersaturated liquid, Int. J. Heat Mass Transf. 23 (3) (1980) 293–299, https://doi.org/10.1016/0017-9310(80)90117-9.

[35] B.C. Donose, F. Harnisch, E. Taran, Electrochemically produced hydrogen bubble probes for gas evolution kinetics and force spectroscopy, Electrochem. Commun. 24 (2012) 21–24, https://doi.org/10.1016/j.elecom.2012.08.009.

[36] Y. Wang, M.E. Zaytsev, H. Le The, J.C.T. Eijkel, H.J.W. Zandvliet, X. Zhang, D. Lohse, Vapor and gas-bubble growth dynamics around laser-irradiated, water-immersed plasmonic nanoparticles, ACS Nano 11 (2) (2017) 2045–2051, https://doi.org/10.1021/acsnano.6b08229.

[37] A. Bashkatov, S.S. Hossain, X. Yang, G. Mutschke, K. Eckert, Oscillating hydrogen bubbles at Pt microelectrodes, Phy. Rev. Lett. 123 (21) (2019) 214503.

[38] H. Matsushima, D. Kiuchi, Y. Fukunaka, Measurement of dissolved hydrogen supersaturation during water electrolysis in a magnetic field, Electrochim. Acta 54 (24) (2009) 5858–5862, https://doi.org/10.1016/j.electacta.2009.05.044.

[39] H. Vogt, K. Stephan, Local microprocesses at gas-evolving electrodes and their influence on mass transfer, Electrochim. Acta 155 (2015) 348–356, https://doi.org/10.1016/j.electacta.2015.01.008.

[40] P.A. Kempler, R.H. Coridan, N.S. Lewis, Effects of bubbles on the electrochemical behavior of hydrogen-evolving Si microwire arrays oriented against gravity, Environ. Eng. Sci. 13 (6) (2020) 1808–1817.

[41] J.A. Leistra, Voltage components at gas evolving electrodes, J. Electrochem. Soc. 134 (10) (1987) 2442, https://doi.org/10.1149/1.2100218.

[42] Y. Li, H. Zhang, T. Xu, Z. Lu, X. Wu, P. Wan, X. Sun, L. Jiang, Under-water superaerophobic pine-shaped Pt nanoarray electrode for ultrahigh-performance hydrogen evolution, Adv. Funct. Mater. 25 (11) (2015) 1737–1744, https://doi.org/10.1002/adfm.201404250.

[43] R. Iwata, L. Zhang, K.L. Wilke, S. Gong, M. He, B.M. Gallant, E.N. Wang, Bubble growth and departure modes on wettable/non-wettable porous foams in alkaline water splitting, Joule 5 (4) (2021) 887–900, https://doi.org/10.1016/j.joule.2021.02.015.

[44] T. Kadyk, D. Bruce, M. Eikerling, How to enhance gas removal from porous electrodes? Sci. Rep. 6 (1) (2016) 38780, https://doi.org/10.1038/srep38780.

[45] H. Vogt, R.J. Balzer, The bubble coverage of gas-evolving electrodes in stagnant electrolytes, Electrochim. Acta 50 (10) (2005) 2073–2079, https://doi.org/10.1016/j.electacta.2004.09.025.

[46] P.J. Sides, C.W. Tobias, Resistance of a planar array of spheres: gas bubbles on an electrode, J. Electrochem. Soc. 129 (12) (1982) 2715–2720, https://doi.org/10.1149/1.2123654.

[47] H. Vogt, The incremental ohmic resistance caused by bubbles adhering to an electrode, J. Appl. Electrochem. 13 (1) (1983) 87–88, https://doi.org/10.1007/BF00615891.

[48] S. Ciampi, K.S. Iyer, Bubbles pinned on electrodes: friends or foes of aqueous electrochemistry? Curr. Opin. Electrochem. 34 (2022) 100992, https://doi.org/10.1016/j.coelec.2022.100992.

[49] V. Haziri, T.P.T. Nha, A. Berisha, J.-F. Boily, A gateway for ion transport on gas bubbles pinned onto solids, Commun. Chem. 4 (1) (2021) 1–5, https://doi.org/10.1038/s42004-021-00481-7.

[50] Y.B. Vogel, C.W. Evans, M. Belotti, L. Xu, I.C. Russell, L.-J. Yu, A.K.K. Fung, N.S. Hill, N. Darwish, V.R. Gonçales, M.L. Coote, K. Swaminathan Iyer, S. Ciampi, The corona of a surface bubble promotes electrochemical reactions, Nat. Commun. 11 (1) (2020) 6323, https://doi.org/10.1038/s41467-020-20186-0.

[51] B. Chmielowiec, T. Fujimura, T. Otani, K. Aoyama, T. Nohira, T. Homma, Y. Fukunaka, A. Allanore, Experimental measurement of overpotential sources during anodic gas formation in aqueous and molten salt systems, J. Electrochem. Soc. 166 (10) (2019) E323–E329, https://doi.org/10.1149/2.1001910jes.

[52] C. Gabrielli, F. Huet, R.P. Nogueira, Fluctuations of concentration overpotential generated at gas-evolving electrodes, Electrochim. Acta 50 (18) (2005) 3726–3736, https://doi.org/10.1016/j.electacta.2005.01.019.

[53] H. Jansen, J. Gardeniers, J. Elders, H. Tilmans, M. Elwenspoek, Applications of fluorocarbon polymers in micromechanics and micromachining, Sens. Actuators A 41 (1–3) (1994) 136–140, https://doi.org/10.1016/0924-4247(94)80101-0.

[54] N. Atthi, J. Supadech, G. Dupuy, O.-u. Nimittrakoolchai, A. Pankiew, S. Supothina, W. Jeamsaksiri, C. Hruanun, A. Poyai, C.-H. Brachais, Increasing active surface area to fabricate ultra-hydrophobic surface by using "black silicon" with bosch etching process, J. Nanosci. Nanotechnol. 12 (6) (2012) 4919–4927, https://doi.org/10.1166/jnn.2012.4906.

[55] J.J. Blackstock, Z. Li, M.R. Freeman, D.R. Stewart, Ultra-flat platinum surfaces from template-stripping of sputter deposited films, Surf. Sci. 546 (2) (2003) 87–96, https://doi.org/10.1016/j.susc.2003.09.039.

[56] Z. Li, P. Beck, D.A.A. Ohlberg, D.R. Stewart, R.S. Williams, Surface properties of platinum thin films as a function of plasma treatment conditions, Surf. Sci. 529 (3) (2003) 410–418, https://doi.org/10.1016/S0039-6028(03)00015-3.

[57] P. Peñas, P. van der Linde, W. Vijselaar, D. van der Meer, D. Lohse, J. Huskens, H. Gardeniers, M.A. Modestino, D. Fernández Rivas, Decoupling gas evolution from water-splitting electrodes, J. Electrochem. Soc. 166 (15) (2019) H769–H776, https://doi.org/10.1149/2.1381914jes.

[58] C. Coutanceau, S. Baranton, T. Audichon, Chapter 3 – hydrogen production from water electrolysis. Hydrogen Electrochemical Production, Academic Press, 2018, pp. 17–62, https://doi.org/10.1016/B978-0-12-811250-2.00003-0.

[59] G. Jerkiewicz, Standard and reversible hydrogen electrodes: theory, design, operation, and applications, ACS Catal. 10 (15) (2020) 8409–8417.

[60] N. Pande, G. Mul, D. Lohse, B. Mei, Correlating the short-time current response of a hydrogen evolving nickel electrode to bubble growth, J. Electrochem. Soc. 166 (10) (2019) E280–E285, https://doi.org/10.1149/2.0191910jes.

[61] C. Gabrielli, F. Huet, M. Keddam, A. Macias, A. Sahar, Potential drops due to an attached bubble on a gas-evolving electrode, J. Appl. Electrochem. 19 (5) (1989) 617–629, https://doi.org/10.1007/BF01320636.

[62] M.Z. Bazant, K. Thornton, A. Ajdari, Diffuse-charge dynamics in electrochemical systems, Phys. Rev. E 70 (2) (2004) 021506, https://doi.org/10.1103/PhysRevE.70.021506.

[63] N. Pande, S.K. Chandrasekar, D. Lohse, G. Mul, J.A. Wood, B.T. Mei, D. Krug, Electrochemically induced pH change: time-Resolved confocal fluorescence microscopy measurements and comparison with numerical model, J. Phys. Chem. Lett. 11 (17) (2020) 7042–7048, https://doi.org/10.1021/acs.jpclett.0c01575.

[64] H. Vogt, The rate of gas evolution of electrodes—I. An estimate of the efficiency of gas evolution from the supersaturation of electrolyte adjacent to a gas-evolving electrode, Electrochim. Acta 29 (2) (1984) 167–173, https://doi.org/10.1016/0013-4686(84)87043-7.

[65] W.S. Cleveland, Robust locally weighted regression and smoothing scatterplots, J. Am. Stat. Assoc. 74 (368) (1979) 829–836, https://doi.org/10.1080/01621459.1979.10481038.

[66] F. Sepahi, N. Pande, K.L. Chong, G. Mul, R. Verzicco, D. Lohse, B.T. Mei, D. Krug, The effect of buoyancy driven convection on the growth and dissolution of bubbles on electrodes, Electrochim. Acta (2021) 139616, https://doi.org/10.1016/j.electacta.2021.139616.

[67] V.M. Volgin, A.V. Zhukov, G.N. Zhukova, A.D. Davydov, Onset of natural convection in the electrochemical cell with horizontal electrodes under non-steady-state conditions: anumerical study, Russ. J. Electrochem. 45 (9) (2009) 1005, https://doi.org/10.1134/S1023193509090055.

[68] X. Yang, D. Baczyzmalski, C. Cierpka, G. Mutschke, K. Eckert, Marangoni convection at electrogenerated hydrogen bubbles, Phys. Chem. Chem. Phys. 20 (17) (2018) 11542–11548, https://doi.org/10.1039/C8CP01050A.

[69] J. Massing, G. Mutschke, D. Baczyzmalski, S.S. Hossain, X. Yang, K. Eckert, C. Cierpka, Thermocapillary convection during hydrogen evolution at microelectrodes, Electrochim. Acta 297 (2019) 929–940, https://doi.org/10.1016/j.electacta.2018.11.187.

[70] A.M. Meulenbroek, A.W. Vreman, N.G. Deen, Competing Marangoni effects form a stagnant cap on the interface of a hydrogen bubble attached to a microelectrode, Electrochim. Acta 385 (2021) 138298, https://doi.org/10.1016/j.electacta.2021.138298.

[71] S. Lubetkin, Thermal Marangoni effects on gas bubbles are generally accompanied by solutal Marangoni effects, Langmuir 19 (26) (2003) 10774–10778, https://doi.org/10.1021/la0358365.

[72] D. Lohse, X. Zhang, Physicochemical hydrodynamics of droplets out of equilibrium, Nat. Rev. Phys. 2 (2020) 426–443, https://doi.org/10.1038/s42254-020-0199-z.

[73] B. Zeng, K.L. Chong, Y. Wang, C. Diddens, X. Li, M. Detert, H.J.W. Zandvliet, D. Lohse, Periodic bouncing of a plasmonic bubble in a binary liquid by competing solutal and thermal marangoni forces, Proc. Natl. Acad. Sci. USA 118 (23) (2021), https://doi.org/10.1073/pnas.2103215118.Publisher: National Academy of Sciences Section: Physical Sciences

[74] D. Baczyzmalski, F. Karnbach, G. Mutschke, X. Yang, K. Eckert, M. Uhlemann, C. Cierpka, Growth and detachment of single hydrogen bubbles in a magnetohydrodynamic shear flow, Phys. Rev. Fluids 2 (9) (2017) 093701, https://doi.org/10.1103/PhysRevFluids.2.093701.

[75] K. Schwarzenberger, T. Köllner, H. Linde, T. Boeck, S. Odenbach, K. Eckert, Pattern formation and mass transfer under stationary solutal Marangoni instability, Adv. Colloid Interface Sci. 206 (2014) 344–371, https://doi.org/10.1016/j.cis.2013.10.003.

[76] A.J. Bard, L.R. Faulkner, Electrochemical Methods: Fundamentals and Applications, second ed., John Wiley & Sons, Inc, 2001.

[77] Á. Moreno Soto, O.R. Enríquez, A. Prosperetti, D. Lohse, D. van der Meer, Transition to convection in single bubble diffusive growth, J. Fluid Mech. 871 (2019) 332–349, https://doi.org/10.1017/jfm.2019.276.

[78] O.R. Enríquez, C. Sun, D. Lohse, A. Prosperetti, D. van der Meer, The quasi-static growth of CO_2bubbles, J. Fluid Mech. 741 (2014) R1, https://doi.org/10.1017/jfm.2013.667.

[79] Á. Moreno Soto, D. Lohse, D. van der Meer, Diffusive growth of successive bubbles in confinement, J. Fluid Mech. 882 (2020) A6, https://doi.org/10.1017/jfm.2019.806.